Modelling of deformation and fracture for a model quasi-brittle material with controlled porosity: Synthetic versus real microstructure

Šavija, Branko; Smith, G.E.; Liu, D; Schlangen, E.; Flewitt, P.E.J.

Modelling of deformation and fracture for a model quasi-brittle material with controlled porosity: Synthetic versus real microstructure

B. Šavija[a,*], G.E. Smith[b], D. Liu[b,c], E. Schlangen[a], P.E.J. Flewitt[b,d]

[a] Microlab, Faculty of Civil Engineering and Geosciences, Delft University of Technology, 2628CN Delft, the Netherlands
[b] Interface Analysis Centre, School of Physics, HH Wills Physics Laboratory, Tyndall Avenue, University of Bristol, Bristol BS8 1TL, United Kingdom
[c] Department of Materials, University of Oxford, Oxford OX1 3PH, United Kingdom
[d] HH Wills Physics Laboratory, School of Physics, University of Bristol, Bristol BS8 1TL, United Kingdom

ABSTRACT

Deformation and fracture of materials are usually considered in terms of brittle and ductile modes. However, there is an intermediate class between these limits that is termed quasi-brittle where there is measurable inelastic deformation prior to final graceful 'brittle' failure. In previous work, we presented deformation and fracture data obtained tests conducted using a model material containing different known amounts of up to about 30% surrogate porosity. The model material is a hemi-hydrate gypsum plaster with additions of expanded polystyrene beads in the size range 1.5–2.0 mm dia. Use of gypsum plaster and artificial "pores" enabled creating a simple brittle model material with isolated pores randomly distributed and their size and geometry controlled. Herein, a comparison between two ways of generating microstructures for computer modelling of deformation and fracture of the model material is presented. The predictions for the computer model have been based upon two microstructure inputs (i) a synthetic 3-D pore model and (ii) measurements of porosity obtained from computed X-ray tomography images of the test material. Predictions of the elastic modulus and tensile strength for the different amount of porosity are compared between the two computer models and the experimental flexural data. The predicted deformation and fracture characteristics that describe the observed quasi-brittle response measured for the model material are discussed.

1. Introduction

Continuum fracture mechanics addresses the relationship between the propagation of a crack or a flaw in a material and the stress state [1]. The fracture of materials is commonly divided into the two categories of ductile and brittle where the former is controlled by plasticity, whilst in the latter fracture occurs with essentially elastic deformation. There is an intermediate category termed quasi-brittle, for materials that show measurable inelastic deformation prior to failure. In general elastic and quasi-brittle fracture are distinguished by the damage that can be introduced into the material. For an elastic material the load-displacement (stress-strain) response in tension follows a continuous rise to peak load followed by unstable fracture. The tensile load-displacement curve for a typical quasi-brittle material is characterised by increasing non-linearity as the peak load is approached, followed by a progressive loss of load-carrying capacity beyond this. The non-linearity in the quasi-brittle load-displacement relationship is associated with the formation of distributed microcracks that at, or close to, the peak load coalesce to form a macrocrack [2,3]. The overall response of the material depends on several microstructural features; for example, the amount of porosity in the material. Materials that fall within the quasi-brittle category include ceramics and ceramic composites, natural rocks, concretes and also synthetic polygranular graphites, which all contain different proportions of pores and aggregates of various sizes and distributions [2,4–6].

---

* Corresponding author.
  E-mail address: b.savija@tudelft.nl (B. Šavija).

Nomenclature

E	Young's modulus (GPa)
G_f	work of fracture (N/mm)
P_v	volumetric porosity (%)
S	normalized strength (–)
u	displacement (mm)
σ	stress (MPa)

The porosity of quasi-brittle materials has a strong influence on mechanical properties and fracture characteristics; both elastic modulus and fracture strength decrease as the pore content increases. These changes in properties are linked closely with the volume fraction of pores, with additional effects of size, shape, orientation and distribution, as observed in materials such as sintered alumina [7], magnesium oxide [8], cement [9], concrete [2–4]. One important material in this category is the synthetic polygranular graphite that is used as a moderator in the core of CO_2 gas cooled nuclear reactors, in which the graphite becomes increasingly porous over the service life due to the radiolytic oxidation that is caused by energy deposition, mainly γ radiation [10]. Various models have been developed to introduce porosity into computer simulations that are designed to predict the effective contributions of pore volume fraction, size, geometry and distribution to the mechanical properties of quasi-brittle materials. To achieve these predictions, the models have been based upon analytical [11–13] and finite element approaches [14,15].

Discrete (i.e. lattice) models have successfully simulated deformation and fracture in quasi-brittle materials such as concrete [16–18], rocks [19,20], and nuclear graphite [21,22]. In these models the material is discretised as a lattice of two-node (spring, truss, or beam) elements that can transfer forces, and crack initiation and propagation is typically simulated by damaging these elements. For recent comprehensive reviews of this class of models and discussion of their relative strengths and weaknesses compared to continuum-based models, the reader is referred to references [23–25]. Meso-scale models of fracture in concrete based on a similar concept were also developed by groups around the world, e.g. [26–28]. These models are capable of easily incorporating microstructural information (i.e. heterogeneity) based on e.g. X-ray computed tomography [29,30]. Herein, one of the most widespread versions of lattice models used in concrete fracture – the Delft lattice model [31,32]- is used. The Delft lattice model was used in the past to successfully simulate fracture in e.g. cementitious materials using X-ray computed tomography images [33–36] or synthetic microstructures [37–39] as an input, providing good predictions compared to experimental data. Note that some other types of models, e.g. discrete element method (DEM) models [40–42] and FE models [43–45], can also be used in combination with micro-CT.

Recently Liu et al. [46] considered a combined experimental and modelling approach that addressed the contribution of porosity in a model porous material with a matrix formed from hemihydrate gypsum plaster, $(CaSO_4 \cdot \frac{1}{2}H_2O)$ and water. Controlled porosity was introduced in the form of expanded spherical polystyrene beads with diameters in the range 1.65–2.0 mm; the beads act as surrogate pores within the bulk gypsum due to their low strength and modulus compared with the matrix, which comprises hydrated calcium sulphate materials as a coherent mass of interlocking needle shaped crystals with less than about 0.5% residual casting porosity [47]. Varying the additions of beads produced a range of model materials with up to about thirty volume percent of added porosity. Rectangular specimens (20 mm × 20 mm × 150 mm) were loaded under four-point bending to record the effect of the increased porosity on the elastic modulus and flexural strength. A 3-D simulation of the porosity in each microstructure was created, assuming a random distribution of spherical pores based upon the size range of polystyrene beads used (i.e. 1.65–2 mm diameter) positioned in the gypsum matrix. This was combined with an assumed 'pore free' elastic modulus and fracture strength of the matrix gypsum and was used as input to the lattice-based multi-scale finite element model to predict the elastic modulus, fracture strength (i.e. modulus of rupture) and also the formation and propagation of cracks. The modelling correctly predicted the trends observed in the experimental results and described micro-crack distributions and final fracture sites at the centimetre length-scale.

In this paper, we have utilised computed X-ray tomography to measure directly the porosity introduced into the model gypsum material of Liu et al. [46]. We apply these data to examine the sensitivity of the lattice-based multi-scale finite element model to pore size distribution and total porosity. Simulations that use the tomography data to describe the pore size and pore arrangements are compared with those that use synthesised porosity, randomly extracted and arranged from the measured pore sizes. The objective is

Fig. 1. Gypsum plaster specimens (about 20 × 20 × 20mm) with different amounts of porosity (measured from tomography images), left to right: 12.9%, 22.6%, 30.4%, and 30.0% [46].

to demonstrate whether synthesised porosity provides a sufficient description of the true pore structures. This is important because simulations may be extended to predict heterogeneous porosity distributions in materials that cannot be directly characterised by tomography, but they are also potentially affected by the assumptions made when developing the porous microstructure. It is necessary, therefore, to verify that models of simulated microstructures demonstrate the same behaviour of directly measured microstructures.

2. Experimental data

The analysis presented in this paper uses data from the experiments presented in the previous work by Liu et al. [46]. The experimental results include X-ray computed tomography measurements of the hemihydrate gypsum plaster model materials that contain up to about 30% porosity (Fig. 1). Expanded polystyrene beads of a known range of diameters were used as a surrogate for porosity. The analysis of tomographic images showed that, for the case when no beads were added to the mix, the specimen was still not pore free (within the detection limit of the technique), and a porosity of the order of 0.5% was measured. Some air bubbles remained as a consequence of the mixing procedure, and the amount of these air bubbles in the gypsum matrix was consistent between specimens [46].

The mechanical property data from four point bending loaded beams, which had dimensions of 20 × 20 × 150 mm and a span of 128 mm, are given in Tables 1 and Fig. 2. There is considerable variability between samples of the same nominal porosity, but there is a clear relationship between the elastic modulus and strength for the specimens with added porosity (Fig. 3), but the material without added porosity has a significantly higher strength than material with added porosity (c.f. 12.9% porosity, sample 3) that has similar modulus. Here the elastic modulus values for the nominally pore free material are lower with respect to the measured fracture strength. However, all specimens with added surrogate porosity obey a simple linear relationship. This is consistent with the more uniform distribution of casting induced pores when the polystyrene bead surrogate pores are present.

3. Computer models

In this section we describe the microstructural models together with the computer models that have been adopted to describe the mechanical properties for the quasi-brittle gypsum paste material containing different amounts of porosity. Here the microstructural models are an input to the latter.

3.1. Synthetic microstructures

The centre co-ordinates and radii for every spherical pore within the model space define the microstructure. The model pores were generated successively; each having a diameter chosen randomly from the experimental pore range (between 1.65 and 2.0 mm in diameter). As each pore was created, random co-ordinates were assigned within the model space for the pore centre. Each new pore was tested to ensure it did not overlap any previous pore and failures were rejected. This process was repeated until the target porosity was achieved. For low volumes of pores, greater variability in pore positions was possible but for 30–40% porosity the constraints affect the positioning and little variability was achievable. Examples of the created microstructures are shown in Fig. 4. The porosity can be discretised onto a regular 3D grid, where the value of each voxel is set to zero or one, determined by whether its centre lies either within a pore or within the material. In the models produced for this work, each volume is a cube 200 × 200 × 200 voxels in dimension, with a voxel size of 100 µm. Fig. 4 shows selected synthetic model cubes with porosity distributed within the volume between 2 vol% and 40 vol%. In this sequence the incremental development of the pore distribution is shown. Pore size distributions for all synthetic microstructures are shown in Fig. 5.

3.2. Tomography generated microstructures

Cube specimens of gypsum plaster of about 20 × 20 × 20 mm (Fig. 1) with different amounts of surrogate porosity (expanded polystyrene beads) were cut from the larger casts, and characterised by X-ray computed tomography [46]. Typical reconstructed images, with increasing amounts of expanded polystyrene beads, are shown in Fig. 6. The reconstructed images have a size of around 1300 × 1300 × 1300 voxels, with a voxel size of 16.54 µm. Pore size distributions of scanned samples are given in Fig. 7. It is clear

Table 1
Mechanical properties of model materials measured by four-point bending tests [46]. The porosity is measured by computed X-ray tomography and includes the polystyrene beads that act as a surrogate for porosity.

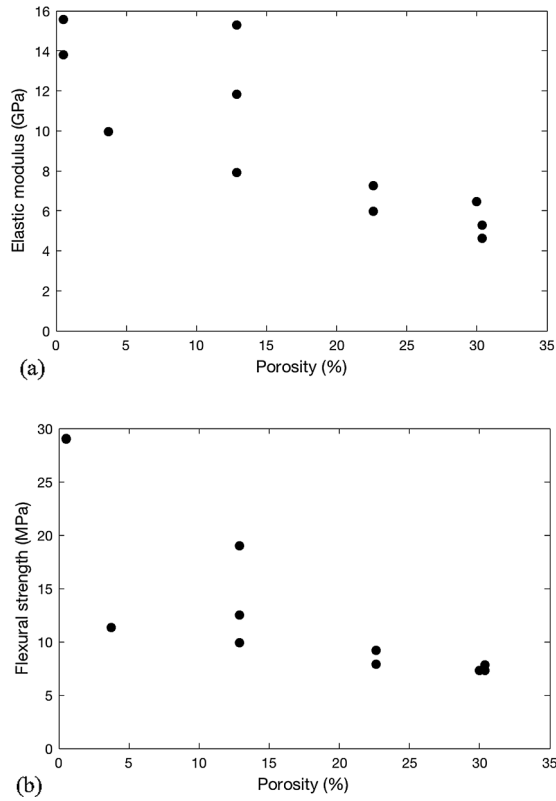| Porosity (%)	Flexural strength (MPa)	Elastic modulus (GPa)
0.5	29.01, 29.04	15.58, 13.80
3.75	11.32	9.97
12.9	9.89, 12.49, 18.98	7.93, 11.81, 15.28
22.6	7.90, 9.18	5.99, 7.27
30	7.28	6.46
30.4	7.31, 7.81	5.28, 4.61

Fig. 2. Porosity/property relationships for the model material measured by four-point bending: (a) elastic modulus; (b) flexural strength.
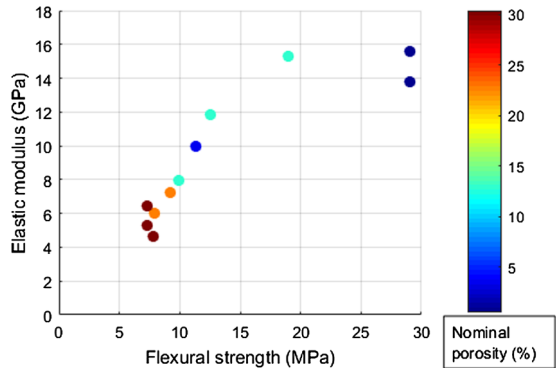

Fig. 3. Relation between flexural strength and elastic modulus for the model quasi-brittle material with varying levels of porosity.

that a certain amount of small pores (termed air bubbles in Fig. 7) are present in each scanned specimen, resulting in a bi-modal porosity distribution. The amount of small pores is relatively constant for all specimens. Note that these are discarded in synthetic microstructures. More information about the pore size distribution and characterization obtained by X-ray tomography is given in [46].

3.3. Multi-scale lattice model

In the model used for the present simulations, a regular cubic lattice grid of Timoshenko beam elements is used for discretization of the solid gypsum plaster material. Pores are empty space. When a load is applied, linear elastic analysis is performed to calculate the response of the lattice mesh. The element with the highest stress-to-strength ratio is then located and removed from the mesh if it exceeds the fracture strength, thereby introducing a small crack (a discontinuity) in the lattice mesh. The analysis is then repeated using this new mesh geometry, with analysis steps repeated until a certain criterion (e.g. maximum load or specimen failure) is achieved. Such an approach is known in the literature as a sequentially-linear approach [48]. Even though local behaviour of each element is brittle, the overall quasi-brittle behaviour of a complex material can be simulated in this simple way.
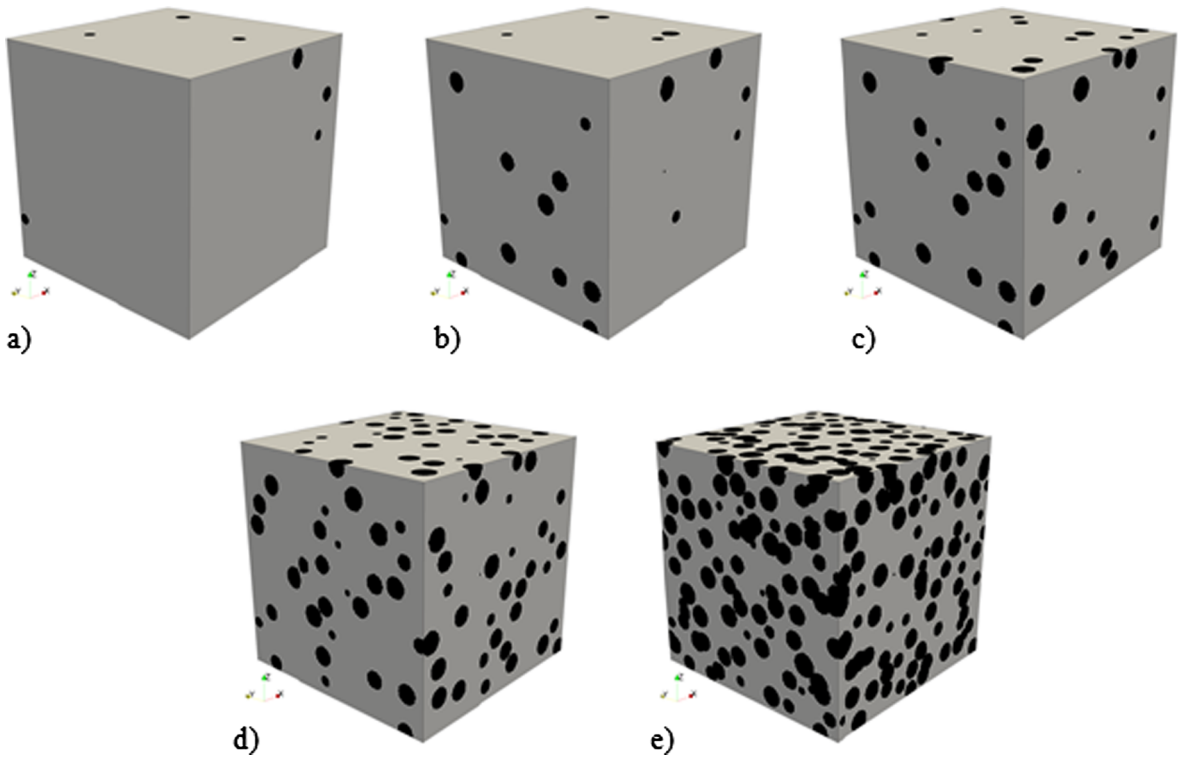
Fig. 4. Computer generated synthetic microstructures (20 × 20 × 20 mm discretised as 200 × 200 × 200 voxels): (a) 2 vol% porosity; (b) 5 vol% porosity; (c) 10 vol% porosity; (d) 20 vol% porosity; and (e) 40 vol% porosity. Grey-solid; black-porosity.
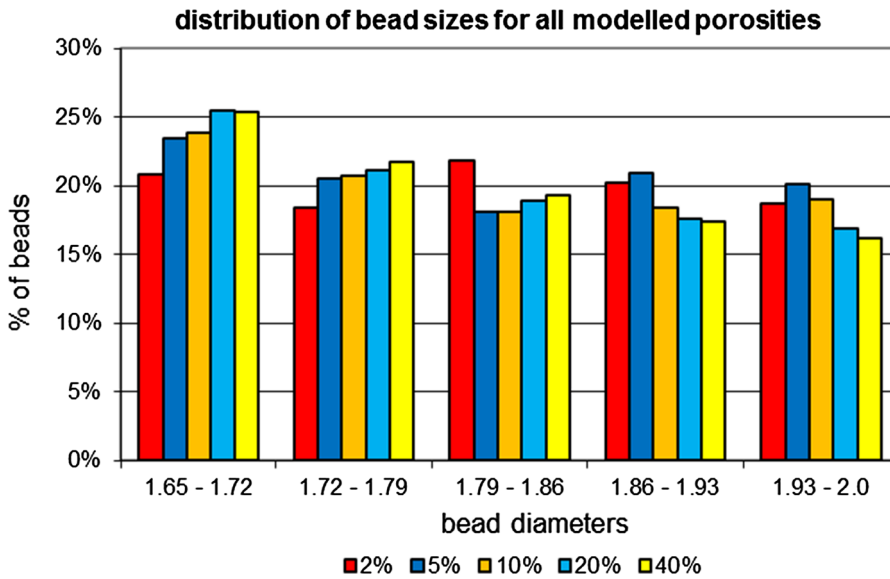

Fig. 5. Distribution of bead sizes in synthetic microstructures for all modelled porosities.

Simulating deformation and fracture in a material with fine microstructural features results in a very high computational demand. Consequently, a multi-scale modelling approach, as previously described in [21,22,46], is used. This is illustrated in Fig. 8, and a brief summary of the approach is provided here. First, the microstructure (such are those shown in Fig. 4) is divided into smaller sub-volumes. A simulated uniaxial tensile test is then performed on each of these sub-volumes; these are referred to as small-scale simulations. In the small-scale simulations (e.g. Fig. 8a), all beam elements locally have linear elastic-ideally brittle behaviour, as described previously [21,22,46]. The small-scale simulations result in a number of stress/strain curves, which are then schematized as multi-linear relationships, (Fig. 8b). As an example, the red curve is a multi-linear schematisation of the black one and has six
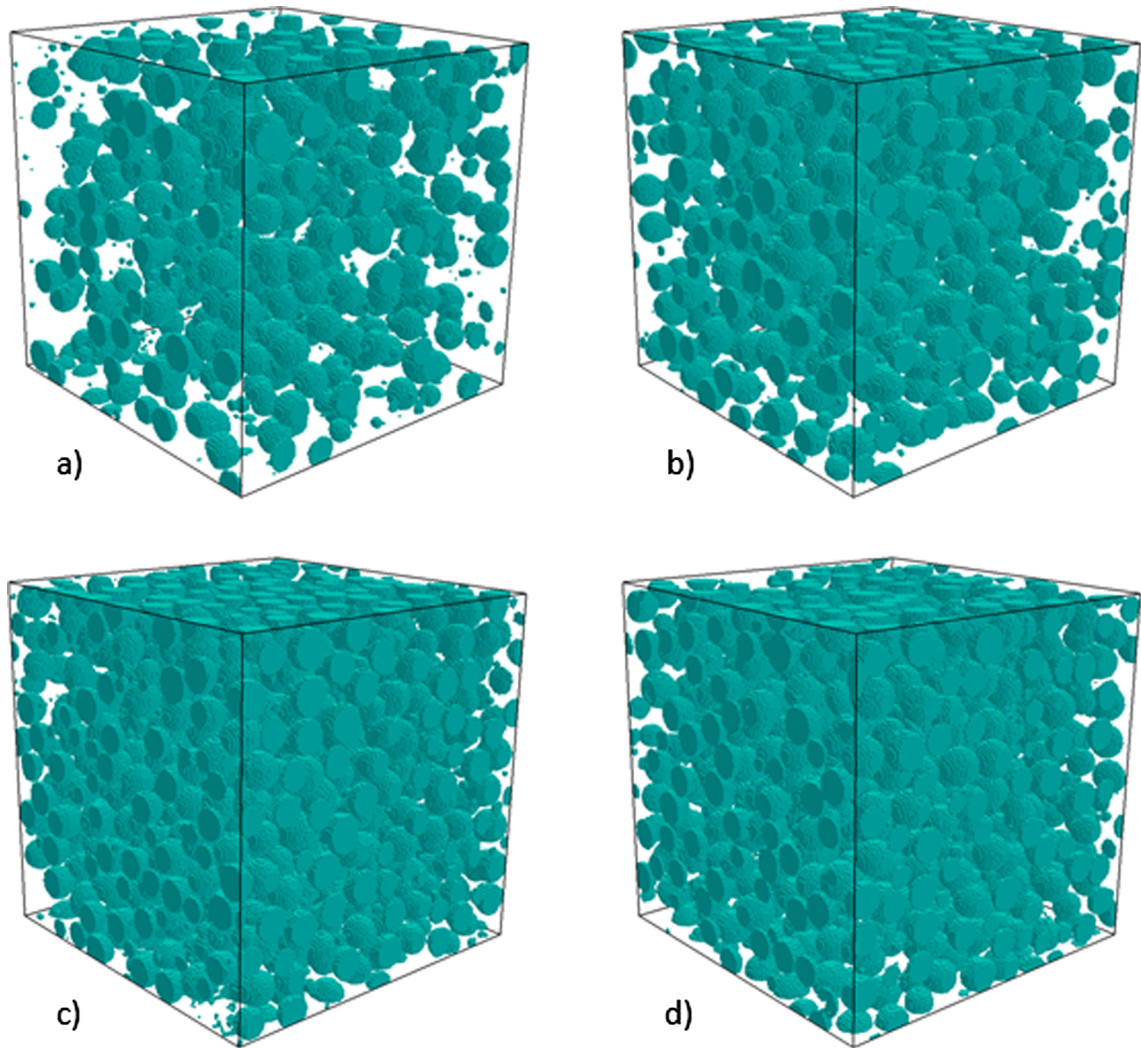
Fig. 6. The reconstructed X-ray tomographic images of the material with total porosity of (a) 12.9 vol%; (b) 22.6 vol%; (c) 30 vol% and (d) 30.4 vol %. Solid particles represent the added expanded polystyrene beads (i.e. the surrogate pores). Small pores are air bubbles produced during manufacture. Reconstructed images shown are $20 \times 20 \times 20$ mm.

segments with points identified as (1) origin; (2) first micro-cracks; (3) peak load; (4) first point in response for which load is < 75% of the peak; (5) first point in response for which the load is < 50% of the peak; (6) first point in response for which the load is < 25% of the peak; (7) point at which load is zero. The multi-linear curves are then used as constitutive relations for beam elements in the larger cube (referred to as full-scale simulations) (Fig. 8c). In the full-scale simulations, the model specimen is also subjected to uniaxial tension. The local element behaviour is not ideally brittle: each element was assigned a multi-linear constitutive relation according to the small-scale simulations. Consequently, an element is not removed in each analysis step, but its stiffness and strength change according to its specific constitutive relation, such that the element will adopt the properties of the next point in the local multi-linear constitutive relation. Consequently, the load-displacement behaviour of the full-scale simulation is obtained (Fig. 8d).[1]

Experiments and simulations of four-point bending have been reported previously [46]. In this work, uniaxial tension simulations are performed. This was done because X-ray computed tomography experiments were performed on cubic specimens as shown in Fig. 1. This means that the simulations cannot be directly compared with the experimental results reported previously. However, in general, a linear relation between tensile and flexural strength is reported for quasi-brittle materials [49]. Therefore, trends observed in the experiments should be captured by the model as well.

The uniaxial tensile behaviour of gypsum plaster with controlled porosity was simulated using the described procedure. The model needs very few parameters as input: the microstructure and the mechanical properties. For the mechanical properties (elastic modulus and tensile strength) of lattice elements, an inverse analysis of the bending experiment involving the gypsum plaster with no

---

[1] Some limitations of the proposed modelling approach are described in the Appendix A.
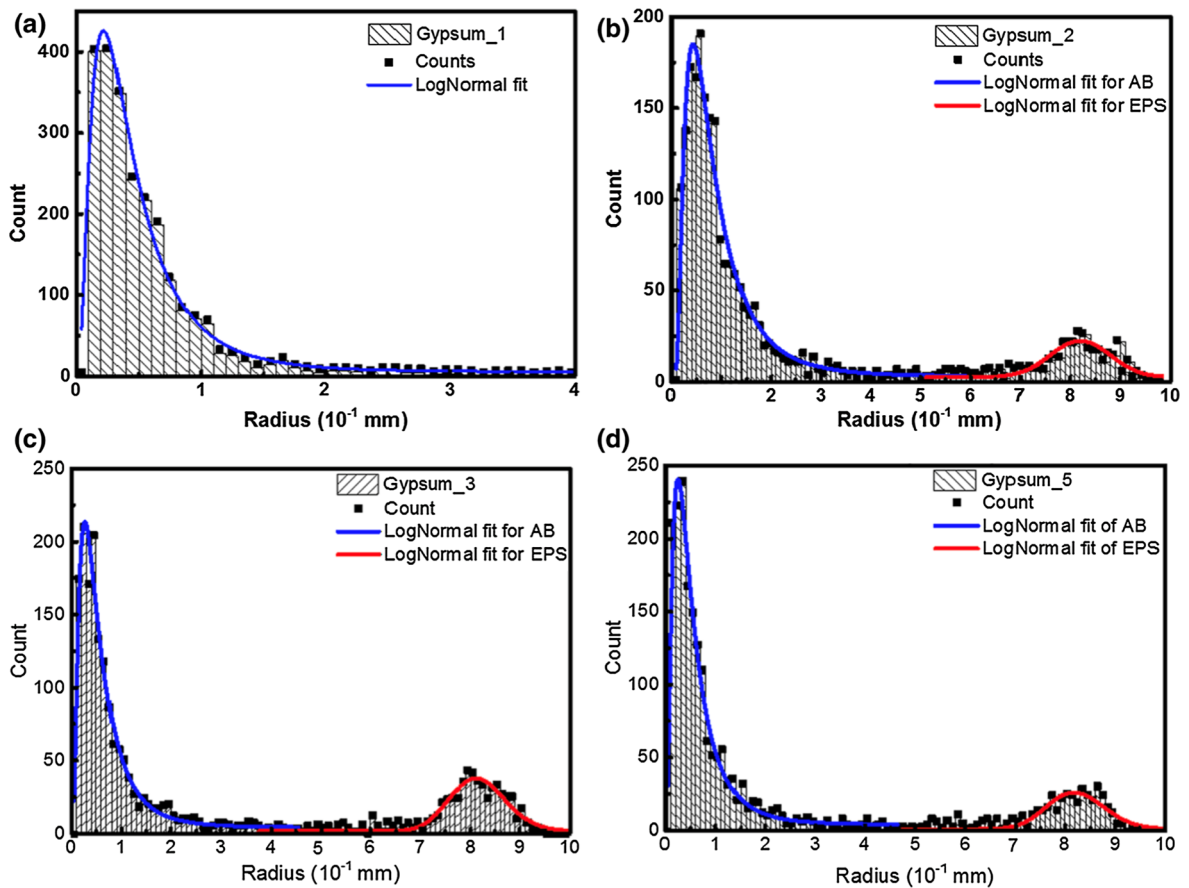
Fig. 7. Distribution of the pores for specimens with a 0.5 vol%; b 12.94 vol%; c 22.56 vol%; d 30.41 vol% porosity. Note the additional distribution of pores between 0.7 and 1.0 mm radius. AB-air bubbles, EPS-polystyrene beads [46].

added porosity was performed[2] [46]. Hence the elastic modulus of the matrix was set to the average modulus of 14.69 GPa (Table 1) and the tensile strength to 17.4 MPa (~60% of the average bending strength of 29 MPa). This ratio is consistent with other quasi-brittle materials such as concrete, where a range between 1 and 3 for flexural vs. tensile strength is commonly reported [50,51]. The exact value of beam element tensile strength was determined in previous work [46] by simulating the four-point bending of the specimen without added porosity.

The model was applied to the microstructures with added surrogate porosity obtained from the tomography images and also to the synthetically generated microstructures. To reduce the computational effort, the resolution of these was reduced. This was done for the segmented tomographic images by increasing the voxel size from 16.0 μm by binning to 95.0 μm. This has a small effect on total porosity (Table 2). The volumes were then cropped to a size of 200 × 200 × 200 voxels. The microstructure was then sliced into cubic sub-volumes (1000 in total). Each resulting cube consisted of 20 × 20 × 20 voxels (Fig. 8a) and was subject to a simulated uniaxial tensile test (Fig. 8b) to obtain a stress-strain relationship. The outputs of these small-scale simulations were used as input for large-scale simulations. The procedure was performed for four microstructures using tomography images as input (porosity between 13.2 vol% and 30.95 vol%), and five synthetic microstructures as input (porosity between 2 vol% and 40 vol%).

Lattice beam element size length equal to the voxel size (i.e. 100 μm for the synthetic microstructure case and 95 μm for the X-ray computed tomography case). For a material with no porosity, each small cube in the simulation has 8000 lattice elements in total. Therefore, the complete (solid) microstructure would have 8000 * 1000 = 80,00,000 lattice beam elements. The total number of lattice elements decreases linearly with porosity (Fig. 9). As explained previously, in small-scale simulations, a single beam with highest stress-to-strength ratio is removed in each analysis step. Therefore, the number of analysis steps can be used as an indication of the computational effort. A relationship between porosity and the number of analysis steps in small-scale simulations is given in Fig. 10. It can be seen that the number of analysis steps is lower for the synthetic input compared to the tomographic input. This is

---

[2] Note that the element tensile strength, determined as described in previous work [46], is not dependent on the lattice element size. This is because, in a regular cubic lattice as used herein, the cross-sectional area of a lattice element is dependent on the size of the voxel related to it. If a smaller beam size would be used, each lattice beam would have a smaller cross-section, and the elastic modulus and the tensile strength would remain the same.
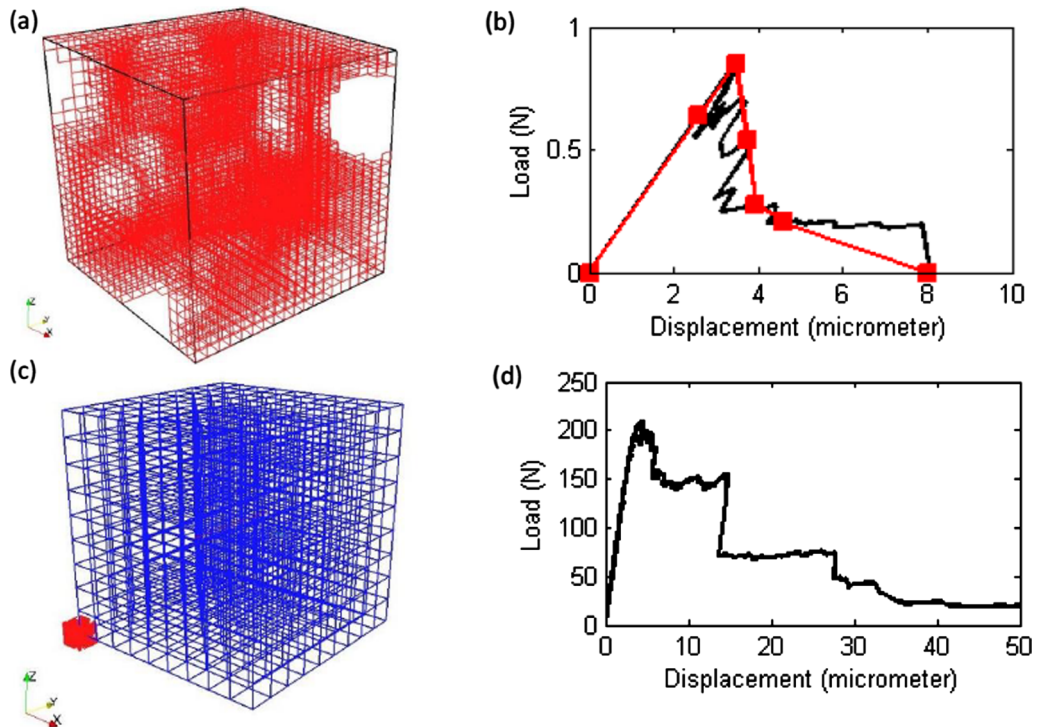
Fig. 8. Multi-scale modelling procedure [46]: (a) lattice discretisation of a small sub-volume, 20 × 20 × 20 voxels; (b) load-displacement curve (black), which is the outcome of a small-scale simulation. (c) detailed mesh shows a small sub-volume (20 × 20 × 20 voxels) in red at its location within the larger volume of a full-scale simulation; (d) example load-displacement curve obtained from the full-scale simulation.

Table 2
Influence of binning on the apparent porosity used as input in the two considered modelling approaches.

Porosity measured by X-ray tomography (16 μm/voxel)	Porosity after binning (95 μm/voxel)
12.9	13.2
22.6	22.5
30.0	30.1
30.4	31.0

because, in synthetic microstructures, small pores resulting from the fabrication process are neglected. These pores result in a relative increase in microcracking before crack localization.

4. Model predictions

Uniaxial stress/strain curves obtained using the multi-scale lattice model are given in Fig. 11 for the tomography (Fig. 11a) and synthetic inputs (Fig. 11b), respectively. For comparison, measurements of two specimens in four-point bending are given in Fig. 12. Note that the test was performed using displacement control, so although the test did not result in catastrophic failure, limited information on the post-peak behaviour was found. Nevertheless, these four-point bending tests indicate that the material becomes more ductile as the porosity increases.

Development of cracks during the test is given in Figs. 14 and 13 for the tomographic and synthetic input, respectively. In addition, the evolution of broken lattice elements with respect to the initial number of lattice elements for each simulation is given in Table 4. The same trend of decreasing brittleness with increasing porosity is observed in the lattice simulations for both input types. However, unlike displacement controlled four-point bending experiments, lattice simulations are able to simulate the post-peak behaviour without difficulty (even the snap-back occurring in some cases). All the simulated specimens exhibit classical quasi-brittle fracture behaviour, that include the linear regime, the non-linear microcracking regime, and the post-peak regime (illustrated schematically in Fig. 15). This is consistent with the behaviour of concrete in uniaxial tension and the conceptional model proposed by van Mier [2], who divided the pre-peak process in two distinct stages: (1) the elastic stage; and the (2) phase of (stable) microcracking. The amount of microcracking will depend, in general, on the specimen microstructure. For a two-phase quasi-brittle
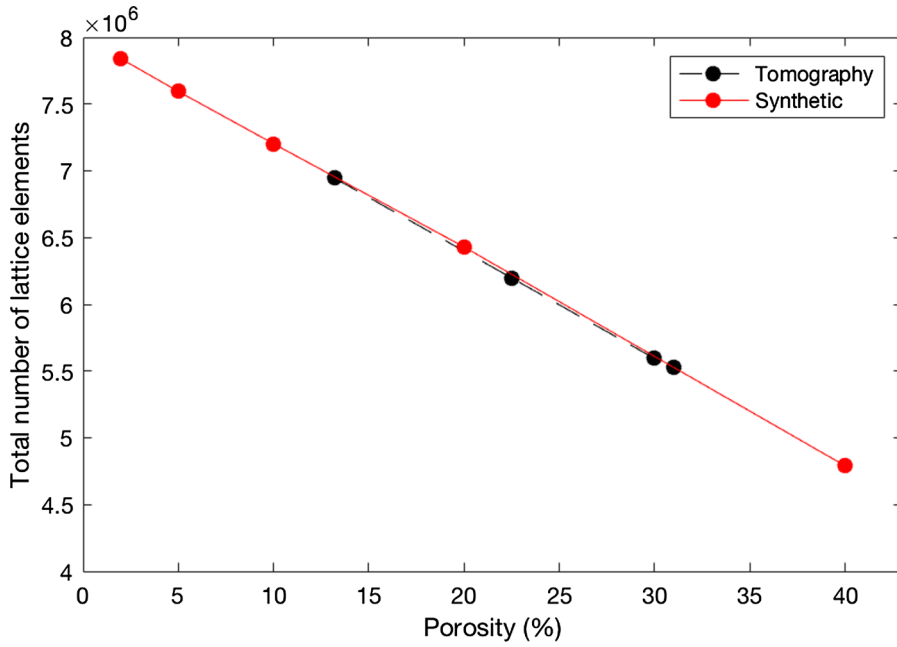
Fig. 9. Decrease in total number of lattice elements with increasing porosity.
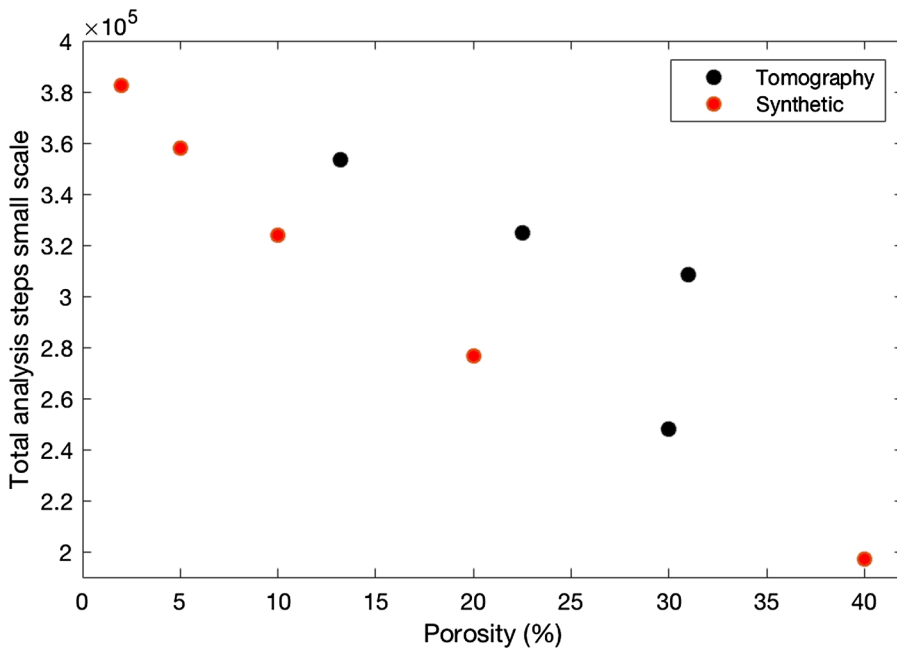

Fig. 10. Comparison between tomographic and synthetic input in terms of computational effort needed for the simulation.

material with relatively large pores as simulated herein, it is expected that limited microcracking will occur before the peak load.

From these curves, the elastic modulus, the tensile strength, and the work of fracture can be obtained. The strength and the modulus both decrease with the increase in porosity. The data for modulus and strength are summarized in Table 3.

Note that the fracture process in multi-phase quasi-brittle materials is a stochastic process [35]. In a material such as that simulated herein, the local distribution of large pores will have a significant effect on the results, especially the strength. In the previous work [46], a clear dependence of the simulation results on the stochastic distribution of pores was found. Note that this effect was more pronounced for the (bending) strength than for the elastic modulus. Furthermore, the effect was more pronounced for lower porosities. For more details, the reader is referred to [46].

In Fig. 15, a schematic load-displacement curve typical of quasi-brittle materials is given. In the curve, three regions can be
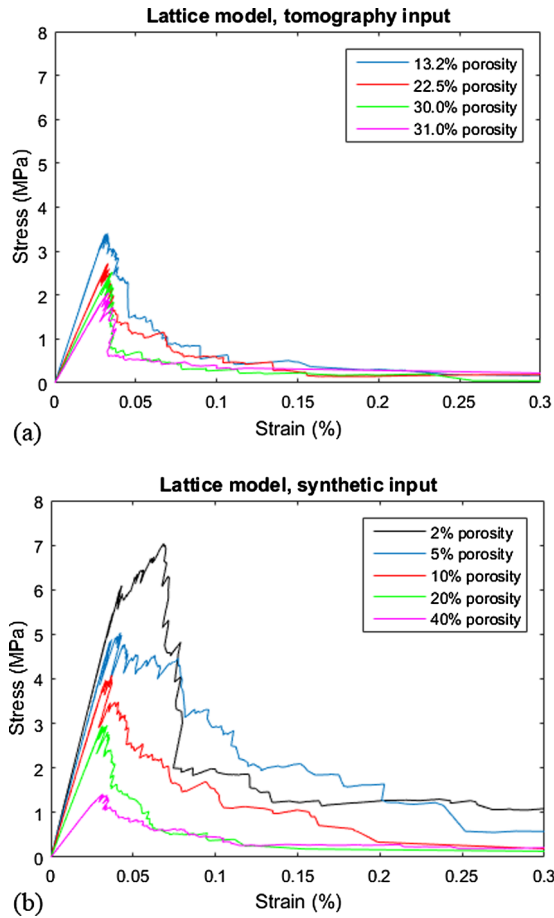
Fig. 11. Uniaxial stress-strain curves for gypsum plaster microstructures with varying levels of porosity obtained using the multi-scale lattice model:
(a) tomography used as input; (b) synthetic microstructures used as input.
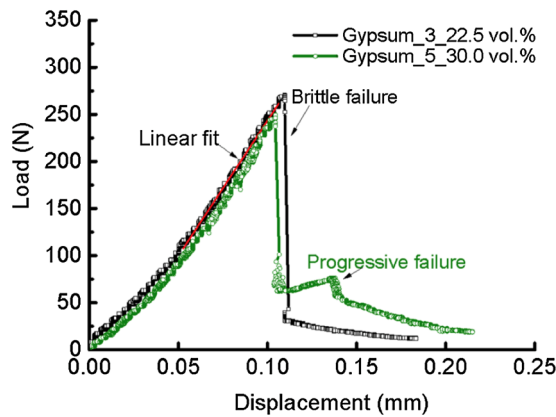
Fig. 12. Load-displacement curves for specimens with 22.5 and 30.0% respectively showing the transition between brittle fracture to progressive
fracture with the increase of porosity [46].

distinguished: the linear elastic region (region I), the non-linear pre-peak region, which is characterized by occurrence of micro-
cracking (region II), and the post-peak softening region (region III). Work of fracture for each region shown in Fig. 15 is calculated
here as:

$$G_f = \int_0^u \sigma du$$

(1)
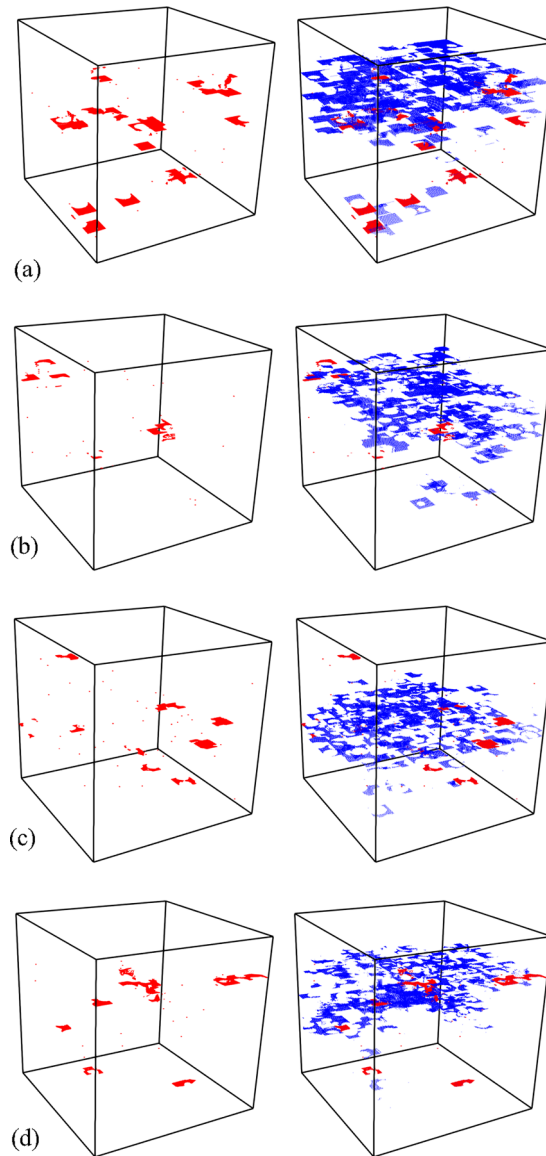
Fig. 13. Crack development in simulated uniaxial tension for the tomographic microstructure specimens with different porosities: (a) 13.2%; (b) 22.5%; (c) 30.1%; and (d) 31.0%. Left – cracks at the peak load; right – cracks at failure (pre-peak cracks shown in red, post peak cracks in blue). Note that loading is applied in the vertical direction. (For interpretation of the references to colour in this figure legend, the reader is referred to the web version of this article.)

where σ is the stress and u the corresponding displacement. The calculated work of fracture for all multi-scale lattice simulations is shown in Table 5, and are summarised in Fig. 16.

5. Discussion

The modelling undertaken in this work has two main objectives. The first objective is to compare the modelling predictions of mechanical properties that use X-ray tomography imaging as input to those that use synthetic (simulated) microstructures as input. For this, a material with a simple microstructure, gypsum, with known additions of surrogate porosity is particularly suitable. It is common in the literature to use simulated microstructures as input in mechanical models [52,53]. It is of critical importance to assess if the simulated microstructure can give predictions comparable to the "real" microstructure, coming from optical images in 2D [54] or X-ray computed tomography in 3D [33,55,56]. The second objective is to describe the fracture mechanisms occurring in the experiments using the models. It is here that the work of fracture provides an instructive measure.
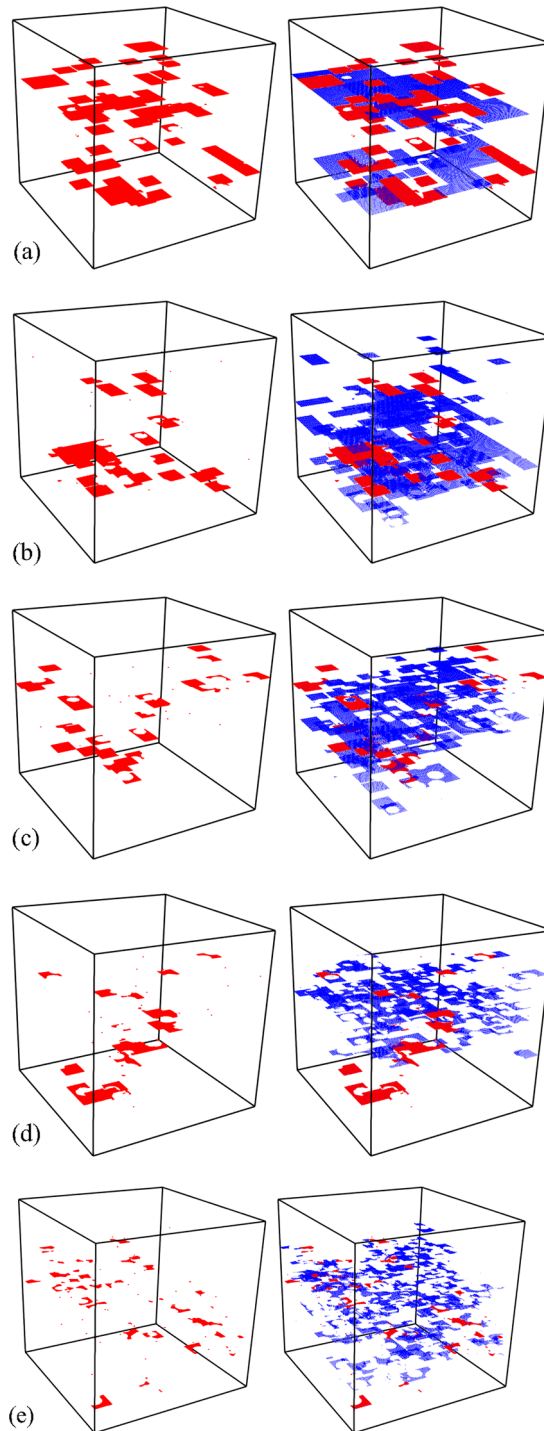
Fig. 14. Crack development in simulated uniaxial tension for the synthetic microstructure specimens with different porosities: (a) 2%; (b) 5%; (c) 10%; (d) 20%; and (e) 40%. Left – cracks at the peak load; right – cracks at failure (pre-peak cracks shown in red, post peak cracks in blue). Note that loading is applied in the vertical direction. (For interpretation of the references to colour in this figure legend, the reader is referred to the web version of this article.)

5.1. Multi-scale lattice model predictions

In this section, modelling predictions of the multi-scale lattice model that use two different types of input microstructure are compared. Furthermore, comparisons are made with experimental data. Note that all simulation results are summarized in Fig. 11
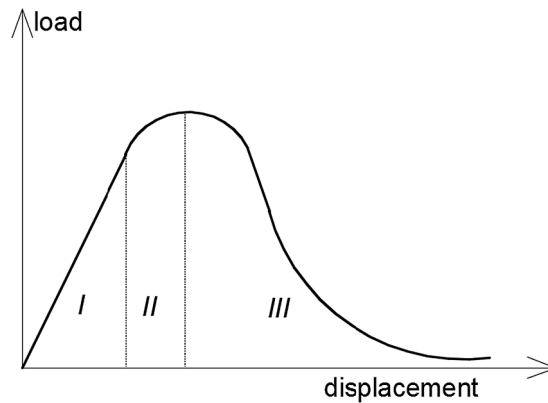
Fig. 15. A schematic load–displacement curve for a quasi-brittle material, region I is linear, region II is non-linear, region III is post peak softening.

Table 3
Summary of lattice simulation results.

Input type	Porosity (vol.%)	Uniaxial tensile strength (MPa)	Elastic modulus (GPa)
Tomography	13.2	3.40	11.11
	22.5	2.72	8.47
	30.1	2.53	7.38
	31.0	2.05	6.44
Synthetic	2	7.04	14.77
	5	5.03	13.63
	10	4.08	12.14
	20	2.96	9.54
	40	1.42	4.79

Table 4
Evolution of the number of fractured lattice beams with respect to their initial number.

Input type	Porosity (vol.%)	Total number of lattice elements	Number of lattice elements failed at peak load	Percentage of lattice elements failed at peak load (%)	Number of lattice elements failed at final stage	Percentage of lattice elements failed at final stage
Tomography	13.2	19,511,511	5891	0.030192	59,878	0.306886
	22.5	17,212,411	1461	0.008488	40,406	0.234749
	30.1	15,343,789	2154	0.014038	35,712	0.232746
	31.0	15,101,137	2655	0.017581	34,931	0.231314
Synthetic	2	22,301,975	30,105	0.134988	76,239	0.341849
	5	21,547,869	11,909	0.055268	85,680	0.397626
	10	20,337,495	8307	0.040846	61,495	0.302373
	20	17,951,584	6016	0.033512	41,350	0.230342
	40	12,994,515	3212	0.024718	37,417	0.287945

Table 5
Work of fracture calculated in lattice simulations.

| Input type	Porosity (vol. %)	Work of fracture (N/mm)						
		Elastic regime (I)-Gf_1	Gf_1/Gf_{tot} (%)	Non-linear regime (II)-Gf_2	Gf_2/Gf_{tot} (%)	Post-peak regime (III)-Gf_3	Gf_3/Gf_{tot} (%)	Total (I + II + III)-Gf_{tot}
Tomography	13.2	0.0034	8.12	0.0012	2.94	0.0372	88.94	0.0418
	22.5	0.0025	8.64	0.0003	1.20	0.0257	90.16	0.0285
	30.1	0.0029	12.41	0.0005	1.96	0.0197	85.63	0.0230
	31.0	0.0028	8.83	0.0004	1.32	0.0282	89.85	0.0314
Synthetic	2	0.0118	9.26	0.0241	18.82	0.0920	71.92	0.1279
	5	0.0069	5.73	0.0045	3.74	0.1091	90.53	0.1205
	10	0.0054	8.31	0.0025	3.86	0.0567	87.83	0.0646
	20	0.0043	11.92	0.0016	4.57	0.0298	83.51	0.0357
	40	0.0007	3.26	0.0005	2.12	0.0217	94.62	0.0229
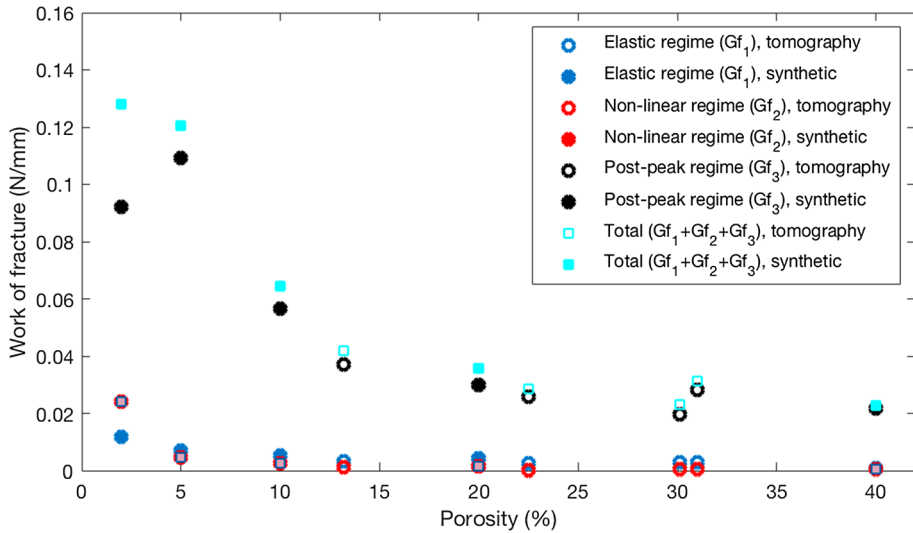
Fig. 16. Effect of porosity on simulated work of fracture when using tomographic images and synthetic microstructures as input (multi-scale lattice model).

and Table 3, and discussed here.

First, simulated elastic modulus was compared to experimental data. Note that four-point bending experiments were performed, while uniaxial tension was simulated because of the shape of specimens that were used for computed tomography.

It can be seen in Fig. 17 that the decrease in elastic modulus with porosity is approximately linear. This is valid for experimental data, but also for both the synthetic and the X-ray tomography microstructures. This is consistent with the literature. For example, Porter and Reed [57] observed a nearly linear drop in elastic modulus with increasing levels of porosity in refractory materials. A similar trend was observed by Dorey et al. [58] for ceramics. Both models seem to be able to reproduce the experimentally measured values of elastic modulus quite well, with minor differences between them, consistent with experimental scatter. The decrease can be described by the following general relation:

$$E = k \cdot P_v + m \tag{2}$$

In Eq. (2), E is the elastic modulus (GPa), P_v the amount of porosity (percentage), k and m are fitting parameters. For experimental data and model predictions, fitting coefficients and coefficient of determination are given in Table 6. In all cases, the predicted data follows an almost perfect linear trend of decrease. There are minor differences in slope between the two input types: the model using synthetic microstructures predicts a marginally steeper decrease compared to the tomography microstructures. This is probably caused by the wider range of porosities considered, rather than any intrinsic differences in the two input types.

Fig. 18 shows a comparison between the experimentally measured and simulated strength of the model material. Note that four-point bending experiments were performed, while uniaxial tension was simulated because of the shape of specimens that were used for computed tomography. Therefore, strength values cannot be compared directly, and have been normalized.

Ideally, samples from the middle region of the beams used in the experiments could be scanned using X-ray computed tomography
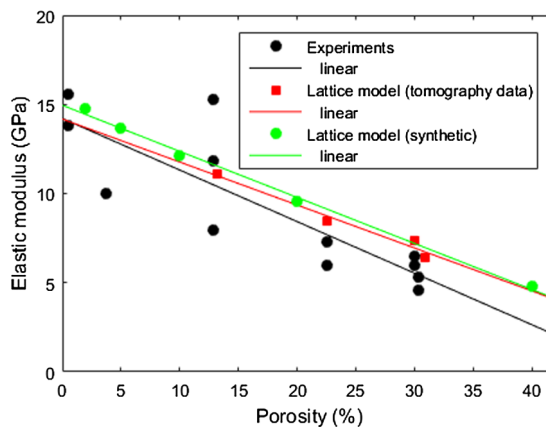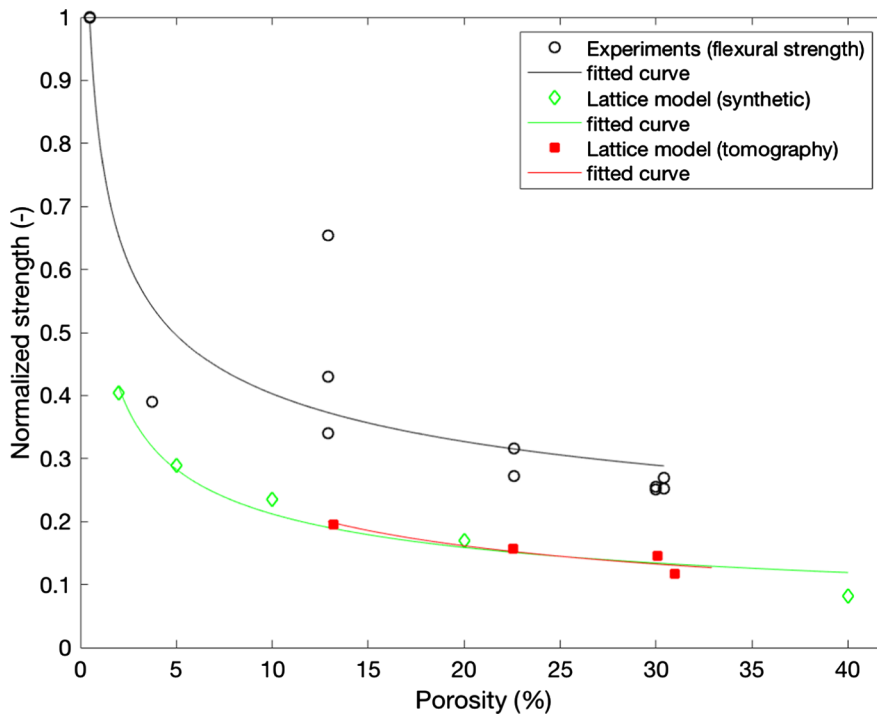

Fig. 17. Comparison of measured elastic modulus with the results of the multi-scale lattice model for different levels of porosity.

Table 6
Fitting coefficients for a linear relation between elastic modulus and porosity (Eq. (2)) for experimental data and multi-scale lattice simulations.

Data	k	m	r^2
Experiments	-0.29	14	0.85
Multi-scale lattice model (tomography)	-0.24	14	0.98
Multi-scale lattice model (synthetic)	-0.26	15	0.99

Fig. 18. Comparison of measured (normalized) strength with the results of the multi-scale lattice model for different levels of porosity.

to characterize the cracks and compare to simulation results. However, since the specimens were loaded until failure, this was not possible. Note that, in our previous work [46], images of the fracture surface of some of the tested specimens are shown, clearly showing the tortuous crack path caused by the induced heterogeneity.

Much like the elastic modulus, the measured values of (bending) strength decrease with increasing porosity (Fig. 18). In Table 1 the flexural strength measured in four-point bending tests shows an exponential decrease from 29 MPa for 0 vol% porosity to 7.3 MPa for 30.4 vol% porosity. This means that the elastic modulus (which shows a nearly linear decrease, as explained above) had a lower reduction within the same porosity range (0–30 vol%) compared to strength: 66% vs. 75% for elastic modulus and bending strength, respectively. This is consistent with the general observation that elastic modulus is less sensitive than strength to increase in porosity [57,58].

Similar to the four-point bending experiments, the multi-scale lattice model predicts a steep decrease for low porosity levels (up to 10%) and then a more gradual decrease. This is further discussed below.

Bai et al. [59] found that a power function can describe a relation between pore porosity and normalized tensile strength measured by Brazillian disc splitting of rock discs. A similar trend was observed by Nott for the tensile strength of analog lithophysal rock [60]. Such a relation is appropriate to correlate the strength calculated using the multi-scale lattice model with the porosity. The

Table 7
Fitting coefficients for a power relation between (normalized) strength and porosity for experimental data and multi-scale lattice simulations.

Data	A	B	r^2
Experiments	0.804	-0.3003	0.933
Multi-scale lattice model (tomography)	0.3398	-0.3066	0.996
Multi-scale lattice model (synthetic)	0.5518	-0.4155	0.982

following general power relation can be used:

$$S = A \cdot P_v^B \tag{3}$$

In Eq. (3), S is the normalized strength, P_v the amount of porosity (percentage), and A and B are fitting parameters. For the experiments and multi-scale lattice model simulations, fitting coefficients and coefficient of determination are given in Table 7.

From Fig. 18 it is clear that there is not much difference between the synthetic microstructure and the tomography input in terms of predicted strength. It is clear, however, that the multi-scale lattice model, predicts a much more significant drop in tensile strength compared to the measured (bending) strength. This seems intuitively logical, because in a direct tension test the whole specimen is under tension and a probability of sampling of a defect is higher than in a four-point bending test, where only the outermost fibre is exposed to the maximum tensile stress. In the previous work by Liu et. al [46], the multi-scale lattice model was used to study the effect of porosity on simulated bending strength of the same material. Note that, there, only the synthetic microstructures were used as input. The (normalized) results can be approximated by a power relation (Eq. (3)), with $A = 0.8601$ and $B = -0.4369$. In Fig. 19, this is plotted and compared to the simulated uniaxial tensile results. It can be seen that the (simulated) drop in uniaxial tensile strength is more pronounced than the simulated drop in flexural strength.

Model predictions that are less sensitive from the type of input used, i.e. whether it was a "real" microstructure or a synthetic (computer generated) microstructure for the case of a simple model material. This holds for all properties tested: tensile strength, elastic modulus, and energy of fracture. This gives confidence that, for more complex materials in the quasi-brittle category such as graphite and concrete, appropriate microstructural models that take consider all important features can be developed and used for prediction of mechanical and fracture properties.

6. Conclusions

In this work, the influence of porosity on mechanical and fracture properties of a simple quasi-brittle model material was studied by means of a multi-scale modelling approach. The influence of using representative computer-generated microstructure as opposed to "real" (i.e. obtained by X-ray computed tomography) microstructure was studied. Based on the presented results, the following conclusions can be drawn:

- Synthetic microstructures, although simplified, result in very similar simulated mechanical and fracture properties for both modelling approaches. Note that this may be different for pores much smaller than the range studied in this work.
- Both modelling approaches predict a linear decrease in elastic modulus with increasing porosity, which is in accordance with the experiments and the literature data.
- The multi-scale lattice modelling approach predicts a power relationship between porosity and uniaxial tensile strength.
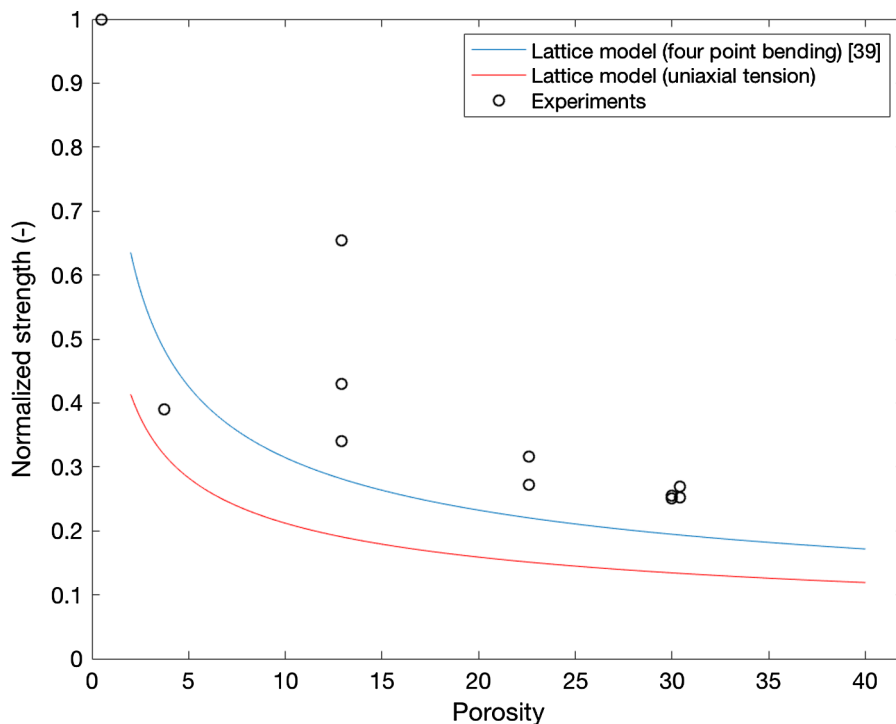

Fig. 19. Comparison of power fits for simulated normalized strength vs. porosity for four-point bending [46] and uniaxial tension.

Qualitatively, this is in accordance with experimental measurements based on four-point bending experiments.

In the presented microstructure model, small pores were not explicitly considered. They were not neglected, though: instead, their influence was addressed in a "smeared" way, i.e. through considering them when determining the elastic modulus and the fracture strength of lattice elements. When simulating materials with fine microstructural features, it is essential to be aware of the limitations of the model: features smaller than the model resolution must be implicitly considered through the constitutive laws of the constituent phases. For a simple model quasi-brittle material, this can be done successfully. Future work will focus on extending and validating the modelling approach on more complex materials, such as graphite and concrete.

Appendix A

Herein, some limitations of the proposed modelling approach are described.

In the multi-scale approach, the microstructure is divided into smaller sub-volumes (see Fig. 8). Simulated global properties are, to a certain extent, dependent on the size of these sub-volumes. This can be shown by simulating a simple 2D example.

Microstructure shown in Fig. 20 consists of two phases: a solid phase and a pore phase. The total microstructure is 200×200 voxels. The following parameters are adopted for the solid phase: elastic modulus of 30 GPa, and the tensile strength of 3 MPa. Three simulations are performed: (1) full simulation, wherein deformation and fracture are simulated using a single-scale approach; (2) multi-scale simulation, with the microstructure sliced in 10×10 sub-volumes (20×20 voxels each); and (3) multi-scale simulation, with the microstructure sliced in 5×5 sub-volumes (40×40 voxels each). A comparison is given in Fig. 21. It can be seen that the multi-scale procedure has almost no effect on the simulated elastic modulus. On the other hand, it does influence the strength and the post-peak response. There are two causes of this: first, stress-strain curves obtained by simulating the sub-volumes are simplified as multi-linear, which has a certain influence on the fracture energy that is passed on to the higher scale; second, slicing of the microstructures induces somewhat different stress-concentrations compared to the full microstructure. This is because the microstructure simulated herein has pores which are randomly distributed, and the microstructure becomes discontinuous by slicing. This issue may be overcome by using overlapping sub-volumes. According to Sencu et al. [61], if the sub-volumes overlap by a certain percentage, sub-volume size will not be an issue. This will be studied in more detail in our future work.

Another issue of using a lattice model with a simple elastic-perfectly brittle material law (as used herein on the smaller scale) is the mesh-size dependence of the response. The influence of beam size on the simulation results has been extensively studied in the past. For a simple case of a 2D uniform triangular lattice, Schlangen and Garboczi [31] showed that a smaller lattice beam size (Fig. 22, higher numbers indicate finer lattice meshes) results in a more brittle post-peak behaviour. This is because in the Delft lattice model the fracture process localizes into the narrowest band permitted by the lattice discretization (which is often one element wide). This is solved in some cases by introducing a discontinuity in the lattice element formulation [27,62]. When such approaches are used, the simplicity of the lattice modelling approach (i.e. a small number of parameters and a simple constitutive law) is lost to a certain extent. As discussed in detail by van Mier [2], lattice models enable a tradeoff between simplicity and precision. A simple lattice model, such as the one chosen herein, enables one to focus on the details of the fracture process without having to use, often phenomenological, parameters. On the other hand, more complex lattice formulations enable one to more accurately mimic the experimental result, albeit at a cost of using numerous non-material parameters.
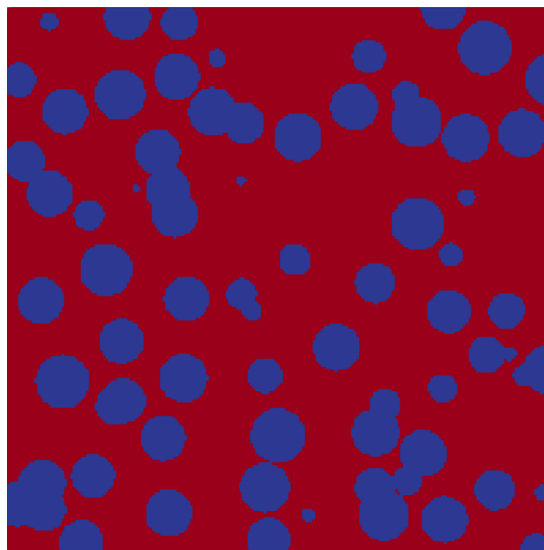

Fig. 20. A 2D microstructure used in the simulations that show the influence of sub-volume size on the simulated global properties. Red-solid; blue-pores. (For interpretation of the references to colour in this figure legend, the reader is referred to the web version of this article.)
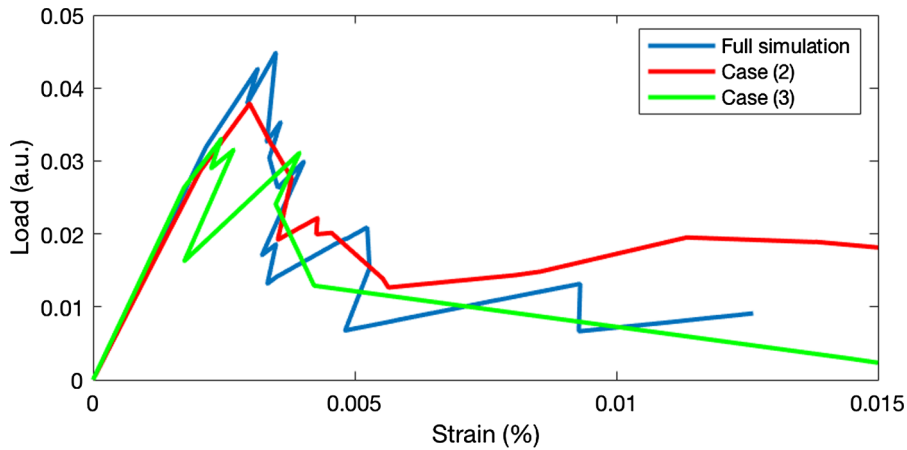
Fig. 21. A comparison between load-strain curves for different cases described.
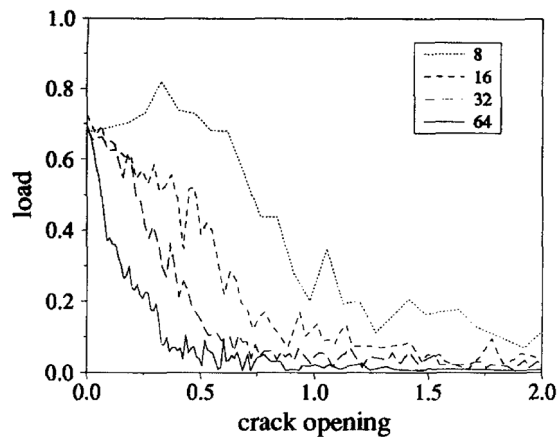

Fig. 22. Load-crack opening and for simulations in which the fineness of the mesh was varied. Load and crack opening displacement units are arbitrary, [31].

Appendix B. Supplementary material

Supplementary data to this article can be found online at https://doi.org/10.1016/j.engfracmech.2018.11.008.

References:

[1] Anderson TL. Fracture mechanics: fundamentals and applications. CRC Press; 2017.
[2] Van Mier JG. Concrete fracture: a multiscale approach. CRC Press; 2012.
[3] Karihaloo BL. Fracture Mechanics and Structural Concrete (Concrete Design and Construction Series). Ed Longman Scientific & Technical United States; 1995.
[4] Bazant ZP, Planas J. Fracture and size effect in concrete and other quasibrittle materials. CRC Press; 1997.
[5] Rice RW. Mechanically reliable ceramics: needs and opportunities to understand and control fracture. J Phys Chem Solids 1984;45:1033–50.
[6] Rice RW. Relation of tensile strength-porosity effects in ceramics to porosity dependence of Young's modulus and fracture energy, porosity character and grain size. Mater Sci Eng, A 1989;112:215–24.
[7] Coble R, Kingery W. Effect of porosity on physical properties of sintered alumina. J Am Ceram Soc 1956;39:377–85.
[8] Spriggs R, Brissette L, Vasilos T. Effect of porosity on elastic and shear moduli of polycrystalline magnesium oxide. J Am Ceram Soc 1962;45. 400-.
[9] Rößler M. Odler I. Investigations on the relationship between porosity, structure and strength of hydrated portland cement pastes I. Effect of porosity. Cem Concr Res 1985;15:320–30.
[10] Hodgkins A, Marrow T, Wootton M, Moskovic R, Flewitt P. Fracture behaviour of radiolytically oxidised reactor core graphites: a view. Mater Sci Technol 2010;26:899–907.
[11] Brown S, Biddulph R, Wilcox P. A strength–porosity relation involving different pore geometry and orientation. J Am Ceram Soc 1964;47:320–2.
[12] Herakovich C, Baxter S. Influence of pore geometry on the effective response of porous media. J Mater Sci 1999;34:1595–609.
[13] Rice R. Evaluation and extension of physical property-porosity models based on minimum solid area. J Mater Sci 1996;31:102–18.
[14] Berre C, Fok S, Mummery P, Ali J, Marsden B, Marrow T, et al. Failure analysis of the effects of porosity in thermally oxidised nuclear graphite using finite element modelling. J Nucl Mater 2008;381:1–8.
[15] Berre C, Fok S, Marsden B, Babout L, Hodgkins A, Marrow T, et al. Numerical modelling of the effects of porosity changes on the mechanical properties of nuclear graphite. J Nucl Mater 2006;352:1–5.

[16] Grassl P, Jirásek M. Meso-scale approach to modelling the fracture process zone of concrete subjected to uniaxial tension. Int J Solids Struct 2010;47:957–68.
[17] Schlangen E, Van Mier J. Experimental and numerical analysis of micromechanisms of fracture of cement-based composites. Cem Concr Compos 1992;14:105–18.
[18] Yip M, Mohle J, Bolander J. Automated modeling of three-dimensional structural components using irregular lattices. Comput-Aided Civ Infrastruct Eng 2005;20:393–407.
[19] Asahina D, Houseworth JE, Birkholzer JT, Rutqvist J, Bolander J. Hydro-mechanical model for wetting/drying and fracture development in geomaterials. Comput Geosci 2014;65:13–23.
[20] Van Mier JG, Schlangen E, Vervuurt A. Tensile cracking in concrete and sandstone: Part 2—effect of boundary rotations. Mater Struct 1996;29:87–96.
[21] Šavija B, Liu D, Smith G, Hallam KR, Schlangen E, Flewitt PE. Experimentally informed multi-scale modelling of mechanical properties of quasi-brittle nuclear graphite. Eng Fract Mech 2016;153:360–77.
[22] Šavija B, Smith GE, Heard PJ, Sarakinou E, Darnbrough JE, Hallam KR, et al. Modelling deformation and fracture of Gilsocarbon graphite subject to service environments. J Nucl Mater 2018;499:18–28.
[23] Nikolić M, Karavelić E, Ibrahimbegovic A, Miščević P. Lattice element models and their peculiarities. Arch Comput Methods Eng 2018;25:753–84.
[24] Pan Z, Ma R, Wang D, Chen A. A review of lattice type model in fracture mechanics: theory, applications, and perspectives. Eng Fract Mech 2018;190:382–409.
[25] Landis EN. Microplanes and microstructure: connecting abstractions and reality. Eng Fract Mech 2018.
[26] Nagai K, Sato Y, Ueda T. Mesoscopic simulation of failure of mortar and concrete by 2D RBSM. J Adv Concr Technol 2004;2:359–74.
[27] Benkemoun N, Hautefeuille M, Colliat JB, Ibrahimbegovic A. Failure of heterogeneous materials: 3D meso-scale FE models with embedded discontinuities. Int J Numer Meth Eng 2010;82:1671–88.
[28] Chen A, Pan Z, Ma R. Mesoscopic simulation of steel rebar corrosion process in concrete and its damage to concrete cover. Struct Infrastruct Eng 2017;13:478–93.
[29] Landis E, Bolander J. Explicit representation of physical processes in concrete fracture. J Phys D Appl Phys 2009;42:214002.
[30] Zhang M, Jivkov AP. Micromechanical modelling of deformation and fracture of hydrating cement paste using X-ray computed tomography characterisation. Compos B Eng 2016;88:64–72.
[31] Schlangen E, Garboczi E. Fracture simulations of concrete using lattice models: computational aspects. Eng Fract Mech 1997;57:319–32.
[32] Lilliu G, van Mier JG. 3D lattice type fracture model for concrete. Eng Fract Mech 2003;70:927–41.
[33] Zhang H, Šavija B, Figueiredo SC, Schlangen E. Experimentally validated multi-scale modelling scheme of deformation and fracture of cement paste. Cem Concr Res 2017;102:175–86.
[34] Schlangen E. Crack development in concrete, part 2: modelling of fracture process. Key Engineering Materials 2008:73–6.
[35] Zhang H, Šavija B, Schlangen E. Towards understanding stochastic fracture performance of cement paste at micro length scale based on numerical simulation. Constr Build Mater 2018;183:189–201.
[36] Zhang H, Šavija B, Luković M, Schlangen E. Experimentally informed micromechanical modelling of cement paste: an approach coupling X-ray computed tomography and statistical nanoindentation. Compos B Eng 2019;157:109–22.
[37] Luković M, Šavija B, Schlangen E, Ye G, van Breugel K. A 3D lattice modelling study of drying shrinkage damage in concrete repair systems. Materials 2016;9:575.
[38] Qian Z, Schlangen E, Ye G, van Breugel K. Modeling framework for fracture in multiscale cement-based material structures. Materials 2017;10:587.
[39] Luković M, Šavija B, Ye G, Schlangen E, van Breugel K. Failure modes in concrete repair systems due to ongoing corrosion. Adv Mater Sci Eng 2017;2017.
[40] Nitka M, Tejchman J. Modelling of concrete fracture at aggregate level using FEM and DEM based on X-ray μCT images of internal structure. Eng Fract Mech 2015;147:13–35.
[41] Suchorzewski J, Tejchman J, Nitka M. Discrete element method simulations of fracture in concrete under uniaxial compression based on its real internal structure. Int J Damage Mech 2018;27:578–607.
[42] Jin C, Yang X, You Z. Automated real aggregate modelling approach in discrete element method based on X-ray computed tomography images. Int J Pavement Eng 2017;18:837–50.
[43] Huang Y, Yang Z, Ren W, Liu G, Zhang C. 3D meso-scale fracture modelling and validation of concrete based on in-situ X-ray Computed Tomography images using damage plasticity model. Int J Solids Struct 2015;67:340–52.
[44] Qsymah A, Sharma R, Yang Z, Margetts L, Mummery P. Micro X-ray computed tomography image-based two-scale homogenisation of ultra high performance fibre reinforced concrete. Constr Build Mater 2017;130:230–40.
[45] Wang X, Yang Z, Yates A, Jivkov A, Zhang C. Monte Carlo simulations of mesoscale fracture modelling of concrete with random aggregates and pores. Constr Build Mater 2015;75:35–45.
[46] Liu D, Šavija B, Smith GE, Flewitt PE, Lowe T, Schlangen E. Towards understanding the influence of porosity on mechanical and fracture behaviour of quasi-brittle materials: experiments and modelling. Int J Fract 2017;205:57–72.
[47] Vekinis G, Ashby M, Beaumont P. Plaster of Paris as a model material for brittle porous solids. J Mater Sci 1993;28:3221–7.
[48] Schlangen E, Qian Z. 3D modeling of fracture in cement-based materials. J Multiscale Modell 2009;1:245–61.
[49] Sorelli L, Meda A, Plizzari G. Bending and uniaxial tensile tests on concrete reinforced with hybrid steel fibers. J Mater Civ Eng 2005;17:519–27.
[50] Maalej M, Li VC. Flexural/tensile-strength ratio in engineered cementitious composites. J Mater Civ Eng 1994;6:513–28.
[51] Monteiro P, Mehta P. Concrete: structure, properties, and materials. Englewood Cliffs: Prentice-Hall; 1993.
[52] Šavija B, Luković M, Pacheco J, Schlangen E. Cracking of the concrete cover due to reinforcement corrosion: a two-dimensional lattice model study. Constr Build Mater 2013;44:626–38.
[53] Qian Z, Garboczi E, Ye G, Schlangen E. Anm: a geometrical model for the composite structure of mortar and concrete using real-shape particles. Mater Struct 2016;49:149–58.
[54] Çopuroğlu O, Schlangen E. Modeling of frost salt scaling. Cem Concr Res 2008;38:27–39.
[55] Man H-K, van Mier JG. Size effect on strength and fracture energy for numerical concrete with realistic aggregate shapes. Int J Fract 2008;154:61–72.
[56] Yang Z, Ren W, Sharma R, McDonald S, Mostafavi M, Vertyagina Y, et al. In-situ X-ray computed tomography characterisation of 3D fracture evolution and image-based numerical homogenisation of concrete. Cem Concr Compos 2017;75:74–83.
[57] Porter D, Reed J, Lewis III D. Elastic moduli of refractory spinels. J Am Ceram Soc 1977;60:345–9.
[58] Dorey R, Yeomans J, Smith P. Effect of pore clustering on the mechanical properties of ceramics. J Eur Ceram Soc 2002;22:403–9.
[59] Bai Q-S, Tu S-H, Zhang C. DEM investigation of the fracture mechanism of rock disc containing hole (s) and its influence on tensile strength. Theor Appl Fract Mech 2016;86:197–216.
[60] Nott JA. Tensile strength and failure criterion of analog lithophysal rock; 2009.
[61] Sencu R, Yang Z, Wang Y. An adaptive stochastic multi-scale method for cohesive fracture modelling of quasi-brittle heterogeneous materials under uniaxial tension. Eng Fract Mech 2016;163:499–522.
[62] Benkemoun N, Poullain P, Al Khazraji H, Choinska M, Khelidj A. Meso-scale investigation of failure in the tensile splitting test: Size effect and fracture energy analysis. Eng Fract Mech 2016;168:242–59.